ACCEPTED VERSION

http://hdl.handle.net/2440/73970

Analytical and finite element prediction of Lamb wave scattering at delaminations in quasi-isotropic composite laminates

C.T. Ng[1*], M. Veidt[2], L.R.F. Rose[3], C.H. Wang[4]

1. School of Civil, Environmental & Mining Engineering, The University of Adelaide, Adelaide, SA, 5005, Australia

2. School of Mechanical and Mining Engineering, The University of Queensland, Brisbane, QLD, 4072, Australia

3. Air Vehicles Division, Defence Science and Technology Organisation, Melbourne, VIC, 3207, Bundoora, VIC, 3083, Australia

4. Sir Lawrence Wackett Aerospace Centre, School of Aerospace, Mechanical and Manufacturing Engineering, RMIT University, Australia

Abstract

This paper presents a theoretical and finite element (FE) investigation of the scattering characteristics of the fundamental anti-symmetric (A_0) Lamb wave at delaminations in a quasi-isotropic (QI) composite laminate. Analytical models based on the Mindlin plate theory and Born approximation are presented to predict the A_0 Lamb wave scattering at a delamination, which is modelled as an inhomogeneity, in an equivalent isotropic model of the QI composite laminate. The results are compared with FE predictions, in which the delamination is modelled as a volume split. The equivalent isotropic model and QI composite laminate are used to investigate the feasibility of the common theoretical approach of modelling the delamination as the inhomogeneity. A good correlation is observed between the theoretical solutions and FE results in the forward scattering amplitudes, but there exists a larger discrepancy in the backward scattering amplitudes. The FE results also show that the

---

[*] Corresponding author:

Email address: alex.ng@adelaide.edu.au (C.T. Ng).

fibre direction of the outer laminae has a pronounced influence on the forward and backward scattering amplitudes, which is not predicted by the analytical models.

1 Introduction

The development of structural health monitoring (SHM) techniques has received significant attention in the last decade [1–4]. Different techniques [5–8] have been developed to ensure the safety and reduce maintenance costs of structures. Guided waves (GWs) have demonstrated great potential for damage detection in a wide range of structural elements, including beams [9], pipes [10], metallic plates [11], and, more recently, composite laminates [12–15].

The successful development of GW-based damage detection techniques requires an understanding of GW propagation and scattering characteristics at defects. GWs in plate-like structures are called Lamb waves. In the literature different analytical models have been developed to predict and investigate characteristics of Lamb waves scattering at different types of defects.

Three-dimensional (3D) prediction plays an important role in these studies. Norris and Vemula [16] and Vemula and Norris [17], for example, presented analytical models for flexural wave scattering by a cylindrical defect using Kirchhoff and Mindlin plate theory, respectively. McKeon and Hinders [18] addressed the problem of fundamental symmetric mode (S_0) Lamb wave scattering at a circular through hole using the Kane-Mindlin plate theory. Diligent *et al*. [19] investigated the interaction of the low-frequency S_0 Lamb wave with a circular through hole using FE, analytical and experimental approaches. Diligent *et al*.'s [19] analytical model was based on Kirchhoff plate theory and the mode superposition method. The study specifically focused on the reflected S_0 Lamb wave and the laterally scattered fundamental shear horizontal mode (SH_0) Lamb wave.

Grahn [20] then extended the S_0 Lamb wave scattering model for a circular blind hole by including the mode coupling effect. Cegla *et al*. [21] presented an analytical model to predict the mode coupling effect of Lamb waves scattering at a circular blind hole. The S_0 and SH_0 Lamb waves were modelled using Poisson plate theory, while the A_0 Lamb wave was modelled

using Mindlin plate theory. Analytical solutions in all of these studies have been limited to simple defect geometries, such as cylindrical or elliptical shapes, and only isotropic materials were considered.

In the last decade, the use of fibre-reinforced composite laminates has significantly increased in different engineering industries, such as civil, maritime, automotive and aerospace, due to their light weight and high specific stiffness characteristics. Analytical models of Lamb wave scattering at defects, however, do not exist for composite laminates because of their anisotropic elastic properties. Hence most studies involving Lamb waves in composites rely on FE simulations, and only few investigations have considered 3D Lamb wave scattering characteristics at defects in composite laminates [22-24].

1.1 Three-dimensional finite element simulation of Lamb wave scattering in composite laminates

Recently Veidt and Ng [23] investigated the A_0 Lamb wave scattering characteristics at circular through holes in composite laminates with different stacking sequences. An experimentally verified FE model was used in the study. The scattering directivity patterns (SDPs) proved quite different for QI composite laminates that have the same number of laminae but different stacking sequences. The 3D A_0 Lamb wave scattering characteristics at delaminations were also studied by Ng and Veidt [24]. The study provided an improved physical insight into the scattering phenomena at the delaminations. However, the experimental verification only focused on a limited number of defect diameter to the incident wave wavelength ratios (R).

One of the objectives of the current study is to provide a comprehensive verification of the 3D FE model for a range of R values. Following earlier investigations [13,15,22–25], the A_0 Lamb wave is the focus in this study because of its sensitivity to small defects due to its shorter wavelength compared to S_0 and SH_0 Lamb waves at the same excitation frequency.

1.2 Lamb wave diffraction tomography and composite laminates

QI composite laminates have commonly been used in the engineering industries because of

their capacity to handle multi-axial loads and undefined load paths. They are suitable for conservative industrial design because some elastic properties of QI composite laminates approximate the equivalent isotropic properties in engineering materials. Applications of QI composite laminates include composite mirrors of telescopes [26], aircraft structures [27] and spacecraft structures [28], etc. However, they have not yet been able to be assessed for defects using Lamb wave diffraction tomography, an assessment method which has been proved attractive in the context of SHM as it not only determines the existence and the location of the defect, but can also achieve the defect characterisation. Current development in this method is limited to isotropic materials [29–32]. Those Lamb based techniques, which have been developed for locating damages in QI composite laminates, are based on equivalent isotropic assumption [12,14,33]. However, the extension of Lamb wave diffraction tomography to characterisation of damages in QI composite laminates requires a scattering model that is able to predict Lamb wave scattering characteristics.

In work related to this goal, Wang and Rose [34] modelled a delamination as an inhomogeneity with a reduced bending rigidity over the delamination region. At the delamination region the laminate is separated into an upper and a lower sub-laminate in which the waveguide is divided into two individual sub-waveguides resulting a reduction of the bending rigidity and this will be discussed in detail in Section 3.2. The study showed that the inhomogeneity can predict reflected and transmitted waves from the delamination. However, the study focused on a one-dimensional waveguide only. In composite laminates, the scattering of Lamb waves at delaminations is a more complicated phenomenon. It is an open question whether the inhomogeneity in the equivalent isotropic model can be used to predict the Lamb wave scattering characteristics at delaminations in QI composite laminates.

Therefore the other objective of the current study is to assess the accuracy of the equivalent isotropic model in predicting the scattering characteristics of the A_0 Lamb wave at delaminations in QI composite laminates. The analytical prediction and Born approximation, which are fundamental to Lamb wave diffraction tomography of the equivalent isotropic model are compared with the experimentally verified FE simulations of the QI composite laminate.

The paper is organised as follows. The 3D FE simulation is described in Section 2. The analytical solutions and Born approximation of the equivalent isotropic model for the A_0 Lamb wave scattering at a cylindrical inhomogeneity are presented in Sections 3 and 4, respectively. The results of the scattering characteristics at defects are discussed in Section 5. Finally, conclusions are drawn in Section 6.

2   Three-dimensional finite element simulation

The 3D explicit FE method was employed to simulate the A_0 Lamb wave propagation and scattering at defects in this study. The program ANSYS was used to generate the geometry and perform the meshing of FE models. An aluminium plate, a QI composite laminate and the corresponding equivalent isotropic model $180 \times 180 \times 1.6$ mm^3 in dimension were modelled using the FE method. Eight-noded 3D reduced integration solid brick elements with hourglass control and three degree-of-freedom at each node were used to model these panels.

The aluminium plate was modelled using eight solid brick elements through the thickness of the plate. The QI composite laminate was made by unidirectional carbon/epoxy prepreg laminae with different fibre orientations. Each lamina was modelled using solid brick elements with homogeneous and orthotropic material assumptions. A small stiffness-weighted damping, which is around 0.012%, was used to simulate the damping effect of the QI composite laminate. The value of the damping ratio was estimated based on the experimental measurements, which was found to be the best to simulate the damping effect for Lamb wave propagation in composite laminates. The FE model of the QI composite laminate has been experimentally verified to be able to accurately predict the A_0 Lamb wave propagation and scattering at through holes [23] and delaminations [24], respectively.

The equivalent isotropic model was modelled following the same approach as the aluminium plate, in which the eight solid brick elements were used throughout the thickness of the plate. The excitation signal was a 140 kHz narrowband six-cycle sinusoidal tone burst pulse modulated by a Hanning window. The A_0 Lamb wave was generated by applying out-of-plane displacement to surface nodes covered by a 5 mm diameter half circle transducer as shown in

Fig 1. The transducer was assumed to be located at $r = 90$ mm and $\theta = 180°$. r and θ are the radial and azimuthal coordinates of a polar coordinate system with the origin at the centre of the defect zone as shown in Fig 1.

The wavelengths of the A_0 Lamb wave propagating at $\theta = 0°$ and 140 kHz in the aluminium plate, the QI composite laminate and the equivalent isotropic model are 9.69 mm, 7.93 mm and 8.22 mm, respectively. Measurements of the A_0 Lamb were ensured by monitoring the out-of-plane displacement of nodes located at the mid-thickness ($z = 0$ mm as shown in Fig 1) of the plate, as the S_0 and SH_0 Lamb waves have zero out-of-plane displacement at the mid-thickness location. 36 nodes were monitored at $r = 40$ mm and $0° \leq \theta \leq 360°$ with 10° step increments at the circular monitoring nodes as shown in Fig 1. The distance $r = 40$ mm is many incident wave wavelengths away from the excitation, hence the generated evanescent waves could be ignored.

The study involved conducting two simulations, one for the panel without a defect and one for a panel with a defect. The scattered A_0 Lamb waves were obtained from 36 monitoring locations by calculating the difference between the signal from the intact and the signal from the damaged panel. The SDP was then obtained by calculating the maximum absolute amplitude of the scattered A_0 Lamb waves. All the scattered A_0 Lamb waves were normalised by the maximum absolute amplitude of the incident A_0 Lamb wave at the centre of the defect zone.

FE meshing was well controlled to ensure all elements had very similar sizes. Control is important, since it has been demonstrated that meshing is an issue in studying wave scattering problems, especially for weak scatterers [19], as large variations in element sizes can cause wave scattering and beam steering. The FE models of the intact and damaged panel had identical mesh to ensure all scattered waves were induced by the defect only. Solid elements with $x-y$ plane dimensions around 0.4×0.4 mm^2 were used for all FE models. This ensured that at least 17 nodes existed per wavelength, which had previously proved sufficient to predict the A_0 Lamb wave propagation and scattering at defects in composite laminates accurately [23–24]. All FE simulations were solved by the explicit FE code LS-DYNA.

Circular through holes and delaminations with different diameters were considered in this study. The predicted A_0 scattered Lamb waves were compared with the results obtained from the analytical model and Born approximation. The through holes were created by removing the FE elements as shown in Fig 2a. The delaminations were modelled by separating the FE nodes across the delamination surface by a small distance [24]. The cross section of the delamination region in the FE model is shown in Fig 2b.

3 Analytical model based on Mindlin plate theory

3.1 Basic equations for Lamb waves

According to the Mindlin plate theory [35], the displacement components (u_x, u_y and u_z) of flexural motions can be expressed in Cartesian coordinates as

$$u_x = -z\psi_x(x,y,t), \quad u_y = -z\psi_y(x,y,t), \quad u_z = w(x,y,t) \tag{1}$$

where ψ_x and ψ_y are the rotation components and w is the deflection component. The equations of motion, with plate thickness h and density ρ, in vector notation [36] are

$$D\left\{\nabla\nabla\cdot\boldsymbol{\psi} - \frac{1-\nu}{2}\nabla\times\nabla\times\boldsymbol{\psi}\right\}\rho + \kappa^2 Gh(\nabla w - \boldsymbol{\psi}) - \rho I\ddot{\boldsymbol{\psi}} = \mathbf{m} \tag{2}$$

$$\kappa^2 Gh\nabla\cdot(\nabla w - \boldsymbol{\psi}) - \rho h\ddot{w} = -q \tag{3}$$

where $\boldsymbol{\psi} = [\psi_x, \psi_y]^T$. $\mathbf{m} = [m_x, m_y]^T$ is a vector containing the area density of external bending moments and q is the area density of external vertical force. $\ddot{\boldsymbol{\psi}} \equiv \partial^2\boldsymbol{\psi}/\partial t^2$ and t denotes time. $D = EI/(1-\nu^2)$ is the plate bending stiffness with Young's modulus E and Poisson's ratio ν. $I = h^3/12$ is the moment of inertia. G is the shear modulus and $\kappa = \pi/\sqrt{12}$ is the shear correction factor for accurate representation of the low frequency behaviour [37]. Vemula and Norris [17] showed that the general solutions of harmonic motion in the absence of loads are in the form

$$w = \text{Re}\left[W(x,y)e^{-i\omega t}\right] \tag{4}$$

$$(\psi_x, \psi_y) = \left(\text{Re}\left[\Psi_x(x,y)e^{-i\omega t}\right], \quad \text{Re}\left[\Psi_y(x,y)e^{-i\omega t}\right]\right) \tag{5}$$

and

$$W(x,y,t) = W_1(x,y,t) + W_2(x,y,t) \tag{6}$$

$$\Psi(x,y,t) = \lambda_1 \nabla W_1(x,y,t) + \lambda_2 \nabla W_2(x,y,t) + \nabla \times (\mathbf{e}_z V(x,y,t)) \tag{7}$$

where ω is the angular frequency and $i = \sqrt{-1}$ is the imaginary unit. λ_1 and λ_2 are the frequency dependent coefficients. $\mathbf{e}_z$ is the unit vector in the z direction. The displacement potentials W_1, W_2 and V in Equations (6) and (7) satisfy the Helmholtz equations [17]

$$(\nabla^2 + k_j^2) W_j = 0, \quad j = 1, 2 \tag{8}$$

$$(\nabla^2 + k_3^2) V = 0 \tag{9}$$

The wavenumbers k_1, k_2 and k_3 can be determined as follows

$$k_j^2 = \frac{1}{2}(k_p^2 + k_b^2) \pm \sqrt{k_f^4 + \frac{1}{4}(k_p^2 - k_b^2)^2}, \quad j = 1, 2 \tag{10}$$

$$k_3^2 = \kappa^2 \frac{k_1^2 k_2^2}{k_p^2} \tag{11}$$

where

$$k_b = \omega \sqrt{\frac{\rho}{\kappa^2 G}}, \quad k_p = \omega \sqrt{\frac{\rho(1 - v^2)}{E}}, \quad k_f = \left(\frac{\rho h \omega^2}{D}\right)^{\frac{1}{4}} \tag{12}$$

Once the wavenumbers k_1 and k_2 are obtained, the λ_j in Equation (7) can be determined by $\lambda_j = -1 + k_b^2 k_j^{-2}$ for $j = 1, 2$. For the frequency below the first cut-off frequency $\omega_c = \kappa \sqrt{Gh / \rho I}$, k_1 is a real wavenumber representing the flexural wave. k_2 and k_3 are purely imaginary and represent evanescent waves. In polar coordinates, the deflection potential of an incident wave propagating in the positive x direction at frequency ω can be expressed as [38]

$$W^{(i)}(r,\theta) = \sum_{n=0}^{\infty} \in_n i^n J_n(k_1 r) \cos(n\theta) \tag{13}$$

where the superscript (i) represents the parameters pertaining to the incident wave. $\in_0 = 1$ and $\in_n = 2$ for $n \geq 1$. $J_n(\cdot)$ is the n-th order Bessel function of the first kind.

3.2 Wave scattering at a cylindrical inhomogeneity

Following the wave function expansion method [17–18,20,38], the solutions for displacement potentials W_1, W_2 and V of the scattered wave, which are due to the incident wave [in Equation (13)] scattering at a cylindrical inhomogeneity with radius a, can be expressed in terms of Bessel and Hankel functions in polar coordinates. The scattered wave at $r > a$ and the wave inside the cylindrical inhomogeneity at $r \leq a$ are thus of the form [17,38]

$$W^{(s)} = \sum_{n=0}^{\infty} \left[A_{1n} H_n\left(k_1 r\right) + A_{2n} H_n\left(k_2 r\right) \right] \cos n\theta \tag{14}$$

$$\psi_r^{(s)} = \sum_{n=0}^{\infty} \left[\lambda_1 A_{1n} k_1 H_n'\left(k_1 r\right) + \lambda_2 A_{2n} k_2 H_n'\left(k_2 r\right) + A_{3n} \frac{n}{r} H_n\left(k_3 r\right) \right] \cos n\theta \tag{15}$$

$$\psi_\theta^{(s)} = -\sum_{n=0}^{\infty} \left[\lambda_1 A_{1n} \frac{n}{r} H_n\left(k_1 r\right) + \lambda_2 A_{2n} \frac{n}{r} H_n\left(k_2 r\right) + A_{3n} k_3 H_n'\left(k_3 r\right) \right] \sin n\theta \tag{16}$$

and

$$W^* = \sum_{n=0}^{\infty} \left[A_{1n}^* J_n\left(k_1^* r\right) + A_{2n}^* J_n\left(k_2^* r\right) \right] \cos n\theta \tag{17}$$

$$\psi_r^* = \sum_{n=0}^{\infty} \left[\lambda_1^* A_{1n}^* k_1^* J_n'\left(k_1^* r\right) + \lambda_2^* A_{2n}^* k_2^* J_n'\left(k_2^* r\right) + A_{3n}^* \frac{n}{r} J_n\left(k_3^* r\right) \right] \cos n\theta \tag{18}$$

$$\psi_\theta^* = -\sum_{n=0}^{\infty} \left[\lambda_1^* A_{1n}^* \frac{n}{r} J_n\left(k_1^* r\right) + \lambda_2^* A_{2n}^* \frac{n}{r} J_n\left(k_2^* r\right) + A_{3n}^* k_3^* J_n'\left(k_3^* r\right) \right] \sin n\theta \tag{19}$$

where $H_n(\cdot)$ represents the n-th order Hankel function of the first kind. The superscript asterisk indicates the variables related to the wave transmitted into the cylindrical inhomogeneity. k_1^*, k_2^*, k_3^*, λ_1^* and λ_2^* are calculated based on the geometric or material properties, which depend on the type of defect inside the cylindrical inhomogeneity. A_{1n}, A_{2n}, A_{3n}, A_{1n}^*, A_{2n}^* and A_{3n}^* are unknown expansion coefficients to be calculated from the continuity conditions of displacements, shear forces and bending moments at the boundary between two regions ($r = a$) as shown below [38].

$$W^{(i)} + W^{(s)} = W^*, \quad \psi_r^{(i)} + \psi_r^{(s)} = \psi_r^*, \quad \psi_\theta^{(i)} + \psi_\theta^{(s)} = \psi_\theta^* \tag{20}$$

$$M_r^{(i)} + M_r^{(s)} = M_r^*, \quad M_\theta^{(i)} + M_\theta^{(s)} = M_\theta^*, \quad Q_r^{(i)} + Q_r^{(s)} = Q_r^* \tag{21}$$

where M_r, M_θ and Q_r are the bending moments and shear force, respectively. They can be obtained by

$$M_r = D\left[\frac{\partial \psi_r}{\partial r} + \frac{v}{r}\left(\frac{\partial \psi_\theta}{\partial \theta} + \psi_r\right)\right], \quad M_\theta = \frac{D}{2}(1-v)\left[\frac{\partial \psi_\theta}{\partial r} + \frac{1}{r}\left(\frac{\partial \psi_r}{\partial \theta} + \frac{\psi_\theta}{r}\right)\right] \tag{22}$$

$$Q_r = \kappa^2 Gh\left(\frac{\partial w}{\partial r} + \psi_r\right) \tag{23}$$

Using the boundary conditions as shown in Equations (20) and (21), a system of equations, for every n value, can be obtained for the six unknown expansion coefficients [17]

$$\begin{bmatrix} \mathbf{L}_n & \mathbf{L}_n^* \\ \mathbf{R}_n & \mathbf{R}_n^* \end{bmatrix}\begin{Bmatrix} -\mathbf{A}_n \\ \mathbf{A}_n^* \end{Bmatrix} = \in_n i^n \begin{Bmatrix} \mathbf{T}_n \\ \mathbf{P}_n \end{Bmatrix} \tag{24}$$

The expressions for the vectors and matrices in Equation (24) are given in the Appendix.

In this study the cylindrical inhomogeneity is used to represent a circular through hole and delamination, respectively. The through hole boundary is characterised by traction free surfaces. It only involves the shear forces and bending moments boundary conditions in Equation (21). Equation (24) can thus reduce to

$$-\mathbf{R}_n\mathbf{A}_n = \in_n i^n \mathbf{P}_n \tag{25}$$

As shown in Fig 3, the delamination can be represented by reducing the value of the plate bending stiffness at the inhomogeneity region [34,38]. At the delamination region the composite laminate is split into an upper and a lower sub-laminate with thickness h_u and h_l. As the laminate is separated into two sub-laminate at the delamination region in which the waveguide is divided into two individual sub-waveguides, the bending rigidity at the delamination region can be calculated by $D^* = E(h_u^3 + h_l^3)/12(1-v^2)$. The scattered wave is obtained once the expansion coefficients are determined.

4   Born approximation

Unlike the analytical model shown in Section 3, the Born approximation is also applicable to defects with complex shapes. In the literature most of the Lamb wave diffraction tomography methods for damage characterisation have thus employed the Born approximation [31–32]. In the current study, the Born approximation was used to approximate the scattered A_0 Lamb wave amplitude and is compared with the analytical and experimentally verified FE predictions.

The plate properties of the inhomogeneity region can be expressed in term of those corresponding to the region outside the inhomogeneity as [38]

$$D^* = D(1+\delta_1) \tag{26}$$

$$\kappa^2 Gh^* = \kappa^2 Gh(1+\delta_2) \tag{27}$$

$$\rho I^* = \rho I(1+\delta_3) \tag{28}$$

$$\rho h^* = \rho h(1+\delta_4) \tag{29}$$

where δ_l for $l = 1, 2, 3, 4$ are nonzero within the region of inhomogeneity but vanish out of it. These four plate properties can be used to represent different types of defects. For example, the variation in h and I represents the corrosion thinning in metallic plates and the delamination in composite laminates, respectively. Using the Born approximation, the scattered A_0 Lamb wave at frequency ω can be approximated [38] as

$$W^{(s)} \approx W^B = \iint \left\{ \delta_1 D \Gamma_{\beta\alpha}^{(i)} g_{3\alpha,\beta} + \left[\delta_2 \kappa^2 Gh \left(W_{,\alpha}^{(i)} - \psi_\alpha^{(i)} \right) + \delta_3 \omega^2 \rho I \psi_\alpha^{(i)} \right] g_{3\alpha} \right.$$
$$\left. + \delta_2 \kappa^2 Gh \left(W_{,\alpha}^{(i)} - \psi_\alpha^{(i)} \right) g_{33,\alpha} + \delta_4 \rho h \omega^2 g_{33} \right\} d\xi d\eta \tag{30}$$

where the comma indicates differentiation over subscripts $[\alpha, \beta] = 1, 2$. (ξ, η) represents an arbitrary point within the inhomogeneity region. Γ is the plate theory strain. g_{31}, g_{32} and g_{33} are Green's functions [36]

$$g_{31} = \gamma \frac{\partial H_0(k_1 r')}{\partial x}, \quad g_{32} = \gamma \frac{\partial H_0(k_1 r')}{\partial y}, \quad g_{33} = \gamma \frac{H_0(k_1 r')}{\lambda_1} \tag{31}$$

where $\gamma = i / 4D(k_1^2 - k_2^2)$ and $r' = \sqrt{(x-\xi)^2 + (y-\eta)^2}$. Using the far-field asymptotic approximation of the Hankel function, the scattered wave by the cylindrical inhomogeneity at frequency ω can be represented by

$$W^B(r,\theta) \approx \sqrt{\frac{2}{\pi k_1 r}} e^{i\left(k_1 r - \frac{\pi}{4}\right)} T(\theta) \sum_{l=1}^{4} \delta_l P_l(\theta) \tag{32}$$

where

$$P_1(\theta) = -\gamma \lambda_1 k_1^2 D \left(\cos^2 \theta + \nu \sin^2 \theta \right) \tag{33}$$

$$P_2(\theta) = -\frac{\gamma \kappa^2 Gh(1-\lambda_1)^2}{\lambda_1}\cos\theta \qquad (34)$$

$$P_3(\theta) = \gamma \lambda_1 \rho I \omega^2 \cos\theta \qquad (35)$$

$$P_4(\theta) = \frac{\gamma \rho h \omega^2}{\lambda_1 k_1^2} \qquad (36)$$

$$T(\theta) = 2\pi k_1 a \frac{J_1\left(k_1 a \sqrt{2-2\cos\theta}\right)}{\sqrt{2-2\cos\theta}} \qquad (37)$$

5   Results and discussions

In this section, the results of the analytical model, Born approximation and FE simulations are compared and discussed in a series of case studies. In Section 5.1, the use of the aluminium plate with a circular through hole to assess the accuracy of the FE simulations is described. The success of the FE simulations in predicting the scattered A_0 Lamb wave is assessed by comparing the results of the simulations with the analytical model described in Section 3.2. Sections 5.2 and 5.3 compare the results of the analytical, approximated (based on Born approximation) and experimentally verified FE predictions for delaminations in the equivalent isotropic model and QI composite laminate, respectively.

5.1   Through holes in the aluminium plate

As noted in Section 1, an analytical model of A_0 Lamb wave scattering at delaminations in composite laminates does not exist. Therefore, an analytical model of A_0 Lamb wave scattering at through holes is used to verify the numerical accuracy of the FE simulations conducted as part of this research. The analysis provided a comprehensive verification of the FE model, which was experimentally verified in previous studies [23–24] for a limited number R values.

The material properties of the aluminium are shown in Table 1. The A_0 Lamb waves

scattered by through holes are calculated using the analytical model and the FE simulations. Without loss of generality, a range of R values is considered. The SDP was compared with the analytical and FE results for through holes with R equals 0.82, 1.03 and 1.23, as shown in Figs 4a, 4b and 4c, respectively. The solid lines are calculated from the analytical model as described in Section 3. Results of the FE simulations are indicated by circles for $0° \leq \theta \leq 360°$ with 10° step increments.

It should be noted that all SDPs in this paper are normalised by the maximum absolute amplitude of the incident wave at the centre of the defect zone (as shown in Fig 1) in the intact panel. Very good agreement is found between these two sets of results, which proves the accuracy of the FE simulations. Fig 4 shows that the forward and backward scattered A_0 Lamb waves have similar amplitudes. However, the forward scattering waves tend to have a larger amplitude for increasing R. Fig 5 shows the normalised amplitudes of the forward ($\theta = 0°$) and backward ($\theta = 180°$) scattered A_0 Lamb waves for a range of R values. The amplitudes of the forward and backward scattering increase with similar slope and magnitude for R smaller than 0.45, after which the backward scattering amplitudes increase with a lower rate and slight variation. Fig 5 shows the accuracy of the FE simulations for a range of R values.

5.2 Delaminations in the equivalent isotropic model of the quasi-isotropic composite laminate

This section compares the analytical, approximated and FE results of the A_0 Lamb wave scattering at delaminations in the equivalent isotropic model, which is an approximation to the [45/-45/0/90]$_S$ QI composite laminate. In this section the FE results are used as a reference to study the suitability of representing the delamination by the inhomogeneity in the analytical model and Born approximation.

The delamination diameters considered in this study are comparable to or less than the incident wavelength. This size range is found to be practical in composite laminates [23]. For this damage size multiple internal reflections within the damage area [39], which are not considered in the analytical models, are expected to have only a minimal effect on the FE

results. The QI composite laminate is made of eight Cycom® 970/T300 unidirectional carbon/epoxy prepreg laminae. The thickness of each prepreg lamina is 0.2 mm and the material properties are shown in Table 2. The elastic properties of the equivalent isotropic model are calculated based on the classical laminated plate theory [40] and are shown in Table 3. Density and thickness of the equivalent isotropic model are assumed to be 1517 kg/m^3 and 1.6 mm, respectively, which are the same as the QI composite laminate. Young's modulus 49.3 GPa, shear modulus 3.52 GPa and Poisson's ratio 0.32 are used in the analytical model and Born approximation. The equivalent isotropic elastic properties shown in Table 3 are used in the FE simulations.

Figs 6a and 6b show the A_0 phase and group velocity dispersion curves at $\theta = 0°$. The solid lines are calculated using the analytical model with the equivalent isotropic material properties of the QI composite laminate. The circles and crosses indicate the results obtained by the FE simulations and experimental measurements of the QI composite laminates, respectively. The experimental results of the phase and group velocity dispersion curve were reported in [23–24] and they are also included in Figs 6a and 6b. It was proved that the A_0 phase and group velocities are not sensitive to the fibre orientation in the QI composite laminate [41]. Very good agreement was obtained in all three sets of results, thus validating the approximation of the phase and group velocity in QI composite laminate at low frequencies by the equivalent isotropic model.

Figs 7a, 7b and 7c show the SDP of the A_0 Lamb wave at delaminations, with R equal to 0.85, 1.09 and 1.46, respectively. It is assumed that the delaminations are located at mid-thickness (between fourth and fifth lamina) of the [45/-45/0/90]$_S$ QI composite laminate, in which $D^* = 0.25D$. The analytical, approximated and FE results are indicated by solid lines, dashed lines and circles, respectively. It should be noted that the SDP of the forward and backward scattering amplitudes are displayed with two different scales in each figure.

Very good agreement is observed between analytical and FE results in the forward scattering amplitudes but there is a larger discrepancy in the backward scattering amplitudes. As the reduced bending stiffness at the delamination is only 25% of the intact region, it is

beyond the scope of the Born approximation, in which the defect is assumed to be a weak inhomogeneity. For the forward scattering amplitudes, the Born approximation still has a good estimation of the shape of the SDP, but it underestimates the forward scattering amplitudes in all three cases.

Without loss of generality, Fig 8 shows the forward scattering amplitudes at $\theta = 0°$, 20° and 40° for a range of R values. Solid lines, dashed lines and circles represent the analytical, approximated and FE results of the equivalent isotropic plate, respectively. The FE results of the QI composite laminate, which are indicated by crosses, are also included in Fig 8 but the results will only be discussed in Section 5.3. Good agreement is observed between analytical and FE results of the equivalent isotropic model, especially at $\theta = 0°$, in which these two sets of results are almost identical.

Overall the Born approximation underestimates the forward scattering amplitudes but it well predicts the trend of the forward scattering amplitude. Fig 9 shows the backward scattering amplitudes at $\theta = 180°$, 200° and 220°. Compared to Fig 8, Fig 9 demonstrates that the backward scattering amplitudes oscillate more rapidly with R than the forward scattering amplitudes. The analytical, approximated and FE results of the backward scattering amplitudes have different oscillation patterns. The analytical results have a shape of a sine function ramping upward. The approximated results oscillate between zero and maximum values and have increasing sine function behaviour. The FE results increase with variations. However, the overall trends of all three sets of results increase with R. Comparing the predictions of the forward and backward scattering amplitudes, the inhomogeneity model well represents the delamination in the forward scattering amplitudes, but there is a larger discrepancy in the backward scattering amplitudes. A similar phenomenon was also shown in [34] for delaminations in composite beams. A possible reason causing the discrepancy between the analytical and FE results is the analytical model does not take into account the multiple internal reflections within the delamination region. This is indicated in Fig 9 in which there is a good agreement between the results of the analytical (solid line) and FE model (circles) for R smaller than 0.3. However, the discrepancy between the analytical and FE results increases for

R larger than 0.3 as the effect of multiple reflections within the delamination region becomes more pronounced.

5.3 Delaminations in the quasi-isotropic composite laminate

It has been reported that the fibre orientation has an influence on the low frequency A_0 Lamb wave SDP at defects in composite laminates [23]. This section investigates the use of the equivalent isotropic model to approximate the A_0 Lamb wave SDP at delaminations in the QI composite laminate. Analytical modelling and Born approximation are used to calculate the scattered wave amplitudes in the equivalent isotropic model. The FE simulations, in which each lamina of the QI composite laminate is modelled by a layer of solid elements with an orientation according to the fibre direction, are treated as the reference model. Figs 10a, 10b and 10c show the SDP of the delaminations located at mid-thickness in the QI composite laminate. In each of these figures, the analytical, approximated and FE results are calculated for the same delamination size. However, the wavelengths of the incident A_0 Lamb wave are different in the equivalent isotropic model (8.22 mm) and QI composite laminate (7.93 mm). R_{EI} and R_{QI} are thus used to represent the delamination diameter to incident wave wavelength ratio for the equivalent isotropic model and QI composite laminate in Fig 10, respectively.

Agreement between the analytical, approximated and FE results is not as good as in the case of isotropic model. The main reason is that the analytical and approximated results of the equivalent isotropic model do not include the influence of the fibre orientations on the scattering amplitudes in the QI composite laminate. However, fairly good agreement of the forward and backward scattering amplitudes and patterns is still obtained in all three sets of results, especially between the analytical and FE results.

A further investigation of the forward and backward scattering amplitudes was carried out for a range of delamination diameter to wavelength ratios and the results are shown in Figs 8 and 9, respectively. The FE results of the QI composite laminate are indicated by crosses. The trends of the forward and backward scattering amplitudes are very similar to those in the FE

results of the equivalent isotropic model. However, there is a discrepancy in the scattering amplitudes of these two sets of FE results.

As shown in Figs 8c and 9c, there is a larger discrepancy in the scattering amplitudes between these two sets of FE results at $\theta = 40°$ and $220°$ compared to $\theta = 0°$ and $20°$, and $\theta = 180°$ and $200°$ in Figs 8a and 8b, and Figs 9a and 9b, respectively. This is mainly due to the influence of the fibre orientations in the QI composite laminate. It should be noted that $\theta = 40°$ and $220°$ are approximately aligned with the fibre direction of outer laminae of the $[45/-45/0/90]_S$ QI composite laminate. Generally, the FE results of the composite laminates have larger magnitude in these θ directions for forward and backward scattering amplitudes. This is consistent with the phenomenon reported in [23] in which the outer lamina has larger influence in the scattering amplitudes.

Comparing to the results of the equivalent isotropic model as discussed in Section 5.2, similar discrepancies between the analytical and approximated results of the equivalent isotropic model, and the FE results of the QI composite laminate are observed in the forward and backward scatter amplitude at $\theta = 0°$ and $20°$, and at $\theta = 180°$ and $200°$ but larger discrepancies are obtained for $\theta = 40°$ and $220°$. Overall the equivalent inhomogeneity model is a reasonable approximation for the scattering behaviour at delaminations in the QI composite laminate, especially the trend of the amplitudes for increasing delamination diameter to wavelength ratios and the shape of the scattering patterns.

The A_0 Lamb wave SDPs of the delaminations located between the third and forth lamina of the QI composite laminate are also shown in Fig 11. Cylindrical inhomogeneities with reduced bending stiffness $D^* = 0.30D$ are used in the analytical model and Born approximation. The inhomogeneities behave closer to weak scatterers than those assuming the delaminations located at mid-thickness of the composite laminate. However, mode conversion occurs as the delaminations are asymmetrically located in the QI composite laminate. The FE simulations include the mode conversion effect in the SDP predictions but the analytical model and Born approximation do not account for this effect. This is a current limitation of the Lamb wave diffraction tomography [31–32], in which only a single wave mode is considered in the

image reconstruction of defects.

As shown in Fig 11, the backward scattering amplitudes and patterns are not well predicted by the analytical and approximated results. However, good agreement of the forward scattering patterns is still observed between the analytical, approximated and FE results. It is expected that the analytical and approximated results have worse predictions in the scattering amplitudes if the delaminations are moved further away from the mid-thickness of the QI composite laminate. The results reveal that the mode conversion effect needs to be accounted in Lamb wave based imaging algorithms [13,42], especially for Lamb wave diffraction tomography [31–32], if the delamination is located far away from the mid-thickness of the composite laminates.

6   Conclusions

An investigation of the A_0 Lamb wave scattering at delaminations in the equivalent isotropic mode and QI composite laminate has been presented in this paper. Analytical solutions of the A_0 Lamb wave scattering at through holes in the aluminium plate have been used to provide a comprehensive verification of the accuracy of the FE simulations for a range of R values. The analytical model based on the Mindlin plate theory using wave function expansion and Born approximation, and FE results have been discussed and compared to investigate the feasibility of the common theoretical approach of modelling the delamination as the inhomogeneity.

Overall, the inhomogeneity well represents the delamination in the forward scattering amplitudes but there is a larger discrepancy in the backward scattering amplitudes. Comparing to the results of the equivalent isotropic model, similar discrepancies have been observed between the analytical models using wave function expansion and Born approximation results of the equivalent isotropic model, and the FE results of the QI composite laminate.

For the delaminations in the equivalent isotropic model, very good agreement has been observed between the analytical model using wave function expansion and FE results in the forward scattering amplitudes. Although the Born approximation underestimates the forward

scattering amplitudes, it well estimates the trend of the amplitude for increasing R and the shape of the SDP in the forward scattering. For the backward scattering, the trends of all three sets of results increase with R but with different oscillation patterns.

The fibre direction of the outer laminae has a significant influence on the scattering amplitudes in the QI composite laminate. Although the analytical models using wave function expansion and Born approximation do not account for this effect, the A_0 scattered Lamb wave is still reasonably approximated, especially for the trend of the amplitudes for increasing delamination diameter to wavelength ratios and the shape of the scattering patterns. The study has also highlighted the importance of accounting the mode conversion effect in the Lamb wave diffraction tomography. Current investigations are focusing on extending the Born approximation for transversely isotropic materials to improve the results of scattering amplitudes for QI composite laminates.

Appendix A. Matrices and vectors in the analytical model

The matrices and vectors in Equation **Error! Reference source not found.** are shown as below.

$$\mathbf{L}_n = \begin{bmatrix} H_n(k_1 a) & H_n(k_2 a) & 0 \\ a\lambda_1 k_1 H'_n(k_1 a) & a\lambda_2 k_2 H'_n(k_2 a) & na^2 H_n(k_3 a) \\ n\lambda_1 H_n(k_1 a) & n\lambda_2 H_n(k_2 a) & a^3 k_3 H'_n(k_3 a) \end{bmatrix} \tag{A1}$$

$$\mathbf{L}_n^* = \begin{bmatrix} J_n(k_1^* a) & J_n(k_2^* a) & 0 \\ a\lambda_1^* k_1^* J'_n(k_1^* a) & a\lambda_2^* k_2^* J'_n(k_2^* a) & na^2 J_n(k_3^* a) \\ n\lambda_1^* J_n(k_1^* a) & n\lambda_2^* J_n(k_2^* a) & a^3 k_3^* J'_n(k_3^* a) \end{bmatrix} \tag{A2}$$

$$\mathbf{R}_n = \begin{bmatrix} \alpha_1 & \alpha_2 & Dna^2(1-\nu)\left[H_n(k_3 a) - k_3 a H'_n(k_3 a)\right] \\ \beta_1 & \beta_2 & Da^2(1-\nu)\left[0.5(k_3 a)^2 H_n(k_3 a) + k_3 a H'_n(k_3 a) - n^2 H_n(k_3 a)\right] \\ \gamma_1 & \gamma_2 & \kappa^2 Gna^2 H_n(k_3 a) \end{bmatrix} \tag{A3}$$

$$\mathbf{R}_n^* = \begin{bmatrix} \alpha_1^* & \alpha_2^* & D^* n a^2 (1-\nu)\left[J_n\left(k_3^* a\right) - k_3^* a J_n'\left(k_3^* a\right)\right] \\ \beta_1^* & \beta_2^* & D^* a^2 (1-\nu)\left[0.5\left(k_3^* a\right)^2 J_n\left(k_3^* a\right) + k_3^* a J_n'\left(k_3^* a\right) - n^2 J_n\left(k_3^* a\right)\right] \\ \gamma_1^* & \gamma_2^* & \kappa^2 G n a^2 J_n\left(k_3^* a\right) \end{bmatrix} \tag{A4}$$

$$\mathbf{A}_n = \left\{ A_{1n} \quad A_{2n} \quad A_{3n} \right\}^T, \quad \mathbf{A}_n^* = \left\{ A_{1n}^* \quad A_{2n}^* \quad A_{3n}^* \right\}^T \tag{A5}$$

$$\mathbf{T}_n = \left\{ J_n\left(k_1 a\right) \quad \lambda_1 k_1 a J_n'\left(k_1 a\right) \quad n \lambda_1 J_n\left(k_1 a\right) \right\}^T \tag{A6}$$

$$\mathbf{P}_n = \left\{ \begin{array}{c} D\lambda_1\left[\left(k_1 a\right)^2 J_n\left(k_1 a\right) + (1-\nu)k_1 a J_n'\left(k_1 a\right) - (1-\nu)n^2 J_n\left(k_1 a\right)\right] \\ D n \lambda_1 (1-\nu)\left[J_n\left(k_1 a\right) - k_1 a J_n'\left(k_1 a\right)\right] \\ \kappa^2 G k_1 a \left(1+\lambda_1\right) J_n'\left(k_1 a\right) \end{array} \right\} \tag{A7}$$

where

$$\alpha_i = D\lambda_i\left[\left(k_i a\right)^2 H_n\left(k_i a\right) + (1-\nu)k_i a H_n'\left(k_i a\right) - (1-\nu)n^2 H_n\left(k_i a\right)\right] \tag{A8}$$

$$\beta_i = D n \lambda_i (1-\nu)\left[H_n\left(k_i a\right) - k_i a H_n'\left(k_i a\right)\right] \tag{A9}$$

$$\gamma_i = \kappa^2 G k_i a \left(1+\lambda_i\right) H_n'\left(k_i a\right) \tag{A10}$$

$$\alpha_i^* = D^* \lambda_i^*\left[\left(k_i^* a\right)^2 J_n\left(k_i^* a\right) + (1-\nu)k_i^* a J_n'\left(k_i^* a\right) - (1-\nu)n^2 J_n\left(k_i^* a\right)\right] \tag{A11}$$

$$\beta_i^* = D^* n \lambda_i^* (1-\nu)\left[J_n\left(k_i^* a\right) - k_i^* a J_n'\left(k_i^* a\right)\right] \tag{A12}$$

$$\gamma_i^* = \kappa^2 G k_i^* a \left(1+\lambda_i^*\right) J_n'\left(k_i^* a\right) \tag{A13}$$

References

[1] J.R. Rose, A baseline and vision of ultrasonic guided wave inspection potential. Journal of Pressure Vessel Technology 124 (2002) 273 – 282.

[2] K.V. Yuen, S.K. Au, J.L. Beck, Two-stage structural health monitoring approach for phase I benchmark studies. Journal of Engineering Mechanics, ASCE 130 (2004) 16 – 33.

[3] H. Sohn, C.R. Farrar, F.M. Hernez, J.J. Czarnecki, D.D. Shunk, D.W. Stinemates, B.R. Nadler, A review of structural health monitoring literature: 1996 – 2001, Report No. LA-13976-MS, Los Alamos National Laboratory, Los Alamos, N.M, 2004.

[4] H.F. Lam, C.T. Ng, A probabilistic method for the detection of obstructed cracks of beam-type structures using spatial wavelet transform. Probabilistic Engineering Mechanics 23 (2008) 237 – 245.

[5] J.B. Ihn, F.K. Chang, Pitch-catch active sensing methods in structural health monitoring for aircraft structures. Structural Health Monitoring 7 (2008) 5 – 19.

[6] H.F. Lam, C.T. Ng, The selection of pattern features from structural damage detection using an extended Bayesian ANN algorithm. Engineering Structures 30 (2008) 2762 – 2770.

[7] H.F. Lam, C.T. Ng, A.Y.T. Leung, Multicrack detection on semirigidly connected beams utilizing dynamic data. Journal of Engineering Mechanics, ASCE 134 (2008) 90 – 99.

[8] W.J. Staszewski, S. Mahzan, R. Traynor, Health monitoring of aerospace composite structures – active and passive approach. Composites Science and Technology 69 (2009) 1678 – 1685.

[9] C.T. Ng, M. Veidt, H.F. Lam, Guided wave damage characterisation in beams utilising probabilistic optimisation. Engineering Structures 31 (2009) 2842 – 2850.

[10] D.N. Alleyne, B. Pavalakovic, M.J.S. Lowe, P. Cawley, Rapid long-range inspection of chemical plant pipework using guided waves. Insight 43 (2001) 93 – 96.

[11] P. Wilcox, Omi-directional guided wave transducer arrays for the raid inspection of large areas of plate structures. IEEE Transactions on Ultrasonics, Ferroelectrics and Frequency

Control 50 (2003) 699 – 709.

[12] H. Sohn, G. Par, J.R. Wait, N.P. Limback, C.R. Farrar, Wavelet-based active sensing for delamination detection in composite structures. Smart Materials and Structures 13 (2004) 153 – 160.

[13] C.T. Ng, M. Veidt, A Lamb-wave-based technique for damage detection in composite laminates. Smart Materials and Structures 18 (074006) (2009) 1 – 12.

[14] S. Salamone, I. Bartoli, F. Lanza di Scalea, S. Coccia, Guided-wave health monitoring of aircraft composite panels under changing temperature. Journal of Intelligent Material Systems and Structures 20 (2009) 1079 – 1090.

[15] C.T. Ng, M. Veidt, N. Rajic, Integrated piezoceramic transducers for imaging damage in composite laminates. Proceedings of SPIE 7493(74932M) (2009) 1 – 8.

[16] A.N. Norris, C. Vemula, Scattering of flexural waves on thin plates. Journal of Sound and Vibration 181 (1995) 115 – 125.

[17] C. Vemula, A.N. Norris, Flexural wave propagation and scattering on thin plates using Mindlin theory. Wave Motion 26 (1997) 1 – 12.

[18] J.C.P. McKeon, M. Hinders, Lamb wave scattering from a through hole. Journal of Sound and Vibration 224 (1999) 843 – 862.

[19] O. Diligent, T. Grahn, A. Bostrom, P. Cawley, M.J.S. Lowe, The low-frequency reflection and scattering of the S0 Lamb mode from a circular through-thickness hole in a plate: finite element, analytical and experimental studies. Journal of Acoustical Society of America 112 (2002) 2589 – 2601.

[20] T. Grahn, Lamb wave scattering from a circular partly through-thickness hole in a plate. Wave Motion 37 (2003) 63 – 80.

[21] F.B. Cegla, A. Rohde, M. Veidt, Analytical prediction and experimental measurement for mode conversion and scattering of plate waves at non-symmetric circular blind holes in isotropic plates. Wave Motion 45 (2008) 162 – 177.

[22] W. Ke, M. Castaings, C. Bacon, 3D finite element simulations of an air-coupled ultrasonic

NDT system. NDT&E International 42 (2009) 524 – 533.

[23] M. Veidt, C.T. Ng, Influence of stacking sequence on scattering characteristics of the fundamental anti-symmetric Lamb wave at through holes in composite laminates. Journal of the Acoustical Society of America 129 (2011) 1280 – 1287.

[24] C.T. Ng, M. Veidt, Scatting of fundamental anti-symmetric Lamb wave at delaminations in composite laminates. Journal of the Acoustical Society of America 129 (2011) 1288 – 1296.

[25] K. Diamanti, C. Soutis, J.M. Hodgkinson, Piezoelectric transducer arrangement for the inspection of large composite structures. Composites Part A 38 (2007) 1121 – 1130.

[26] K.P. Kim, R.D. Hale, Composite mirror surface deformation due to lay-up sequences within quasi-isotropic laminates. Optical Engineering 49 (2010) 063002-1-10.

[27] F.C. Campbell, Structural Composite Materials. ASM International, USA (2010).

[28] D.G. Gilmore, Spacecraft Thermal Control Handbook Volume 1: Fundamental Technologies. The Aerospace Press, USA (2002).

[29] T.D. Mast, Wideband quantitative ultrasonic imaging by time-domain diffraction tomography. Journal of Acoustical Society of America 106 (1999) 3061 – 3071.

[30] E.V. Malyarenko, M.K. Hinders, Ultrasonic Lamb wave diffraction tomography. Ultrasonics 39 (2001) 269 – 281.

[31] A.H. Rohde, M. Veidt, L.R.F. Rose, J. Homer, A computer simulation study of imaging flexural inhomogeneities using plate-wave diffraction tomography. Ultrasonics 48 (2008) 6 – 15.

[32] L.R.F. Rose, C.H. Wang, Mindlin plate theory for damage detection: Imaging of flexural inhomogeneities. The Journal of Acoustical Society of America 127 (2010) 754 – 763.

[33] Y.H. Kim, D.H. Kim, J.H. Han, C.G. Kim, Damage assessment in layered composites using spectral analysis and Lamb wave. Composites Part B: Engineering 38 (2007) 800 – 809.

[34] C.H. Wang, L.R.F. Rose, Wave reflection and transmission in beams containing

delamination and inhomogeneity. Journal of Sound and Vibration 264 (2003) 851 – 872.

[35] R.D. Mindlin, Influence of rotator inertia and shear on flexural motions of isotropic, elastic plates. Journal of Applied Mechanics 18 (1951) 31 – 38.

[36] L.R.F. Rose, C.H. Wang, Mindlin plate theory for damage detection: Source solutions. The Journal of Acoustical Society of America 116 (2004) 154 – 171.

[37] K.F. Graff, Wave motion in elastic solids, Clarendon Press, Oxford, 1975.

[38] C.H. Wang, F.K. Chang, Scattering of plate waves by a cylindrical inhomogeneity. Journal of Sound and Vibration 282 (2005) 429 – 451.

[39] T. Hayashi, K. Kawashima, Multiple reflection of Lamb waves at a delamination. Ultrasonics 40 (2002) 193 – 197.

[40] C.T. Sun, S. Li, Three-dimensional effective elastic constants for thick laminates. Journal of Composite Materials 22 (1988) 629 – 639.

[41] L. Wang, F.G. Yuan, Group velocity and characteristic wave curves of Lamb waves in composites: Modeling and experiments. Composites Science and Technology 67 (2007) 1370 – 1384.

[42] V. Giurgiutiu, J.J. Bao, Embedded-ultrasonics structural radar for in situ structural health monitoring of thin-wall structures. Structural Health Monitoring 3 (2004) 121 – 140.

Tables

Table 1. Material properties of the aluminium

E (GPa)	G (GPa)	v	ρ (kg/m^3)
68.9	26	0.33	2700

Table 2. Material properties of the Cycom® 970/T300 prepreg unidirectional carbon/epoxy lamina [24]

E_{11} (GPa)	E_{22} (GPa)	E_{33} (GPa)	G_{12} (GPa)	G_{13} (GPa)	G_{23} (GPa)	v_{12}	v_{13}	v_{23}	ρ (kg/m^3)
128.75	8.35	8.35	4.47	4.47	2.90	0.33	0.33	0.44	1517

Table 3. Equivalent isotropic elastic properties of the [45/-45/0/90]$_S$ QI composite laminate

$\bar{E}_{11}$ (GPa)	$\bar{E}_{22}$ (GPa)	$\bar{E}_{33}$ (GPa)	$\bar{G}_{12}$ (GPa)	$\bar{G}_{13}$ (GPa)	$\bar{G}_{23}$ (GPa)	$\bar{v}_{12}$	$\bar{v}_{13}$	$\bar{v}_{23}$
49.30	49.30	9.92	18.78	3.52	3.52	0.31	0.32	0.32

Figures
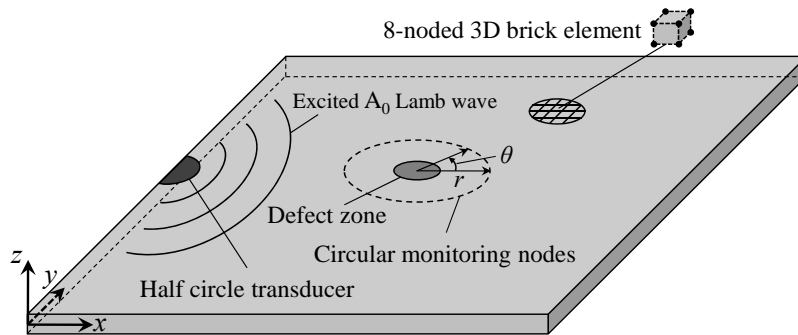
Fig 1. Schematic diagram of the configuration in the FE simulations
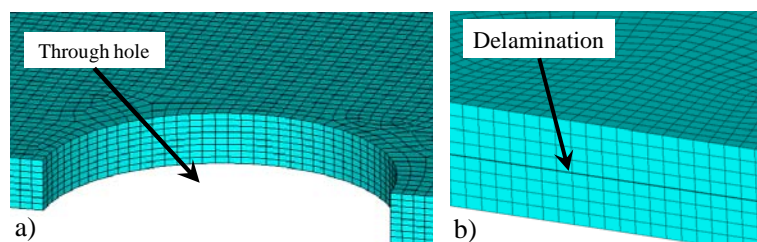
Fig 2. Cross section at (a) a through hole and (b) a delamination in the FE simulations
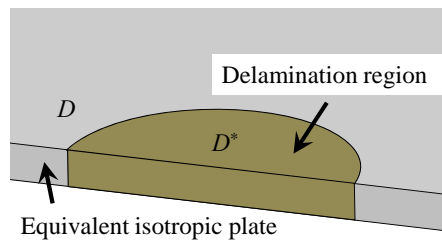
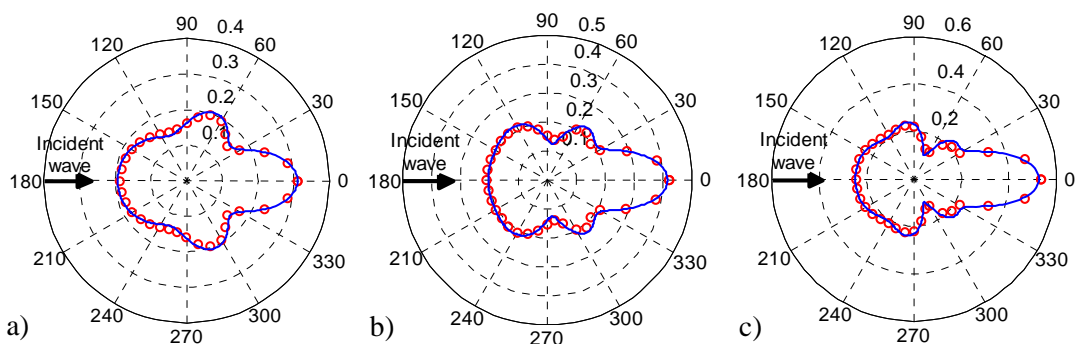Fig 3. Delamination represented by an inhomogeneity in the analytical model

Fig 4. Analytical (solid lines) and FE simulation (circles) results for SDP of through holes with $R=$ (a) 0.82, (b) 1.03 and (c) 1.23 in the aluminium plate
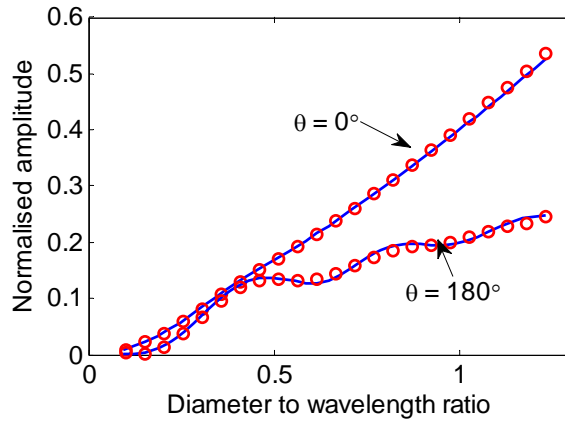
Fig 5. Analytical (solid lines) and FE (circles) results for the normalised forward and backward scattered wave amplitudes as a function of R in the aluminium plate
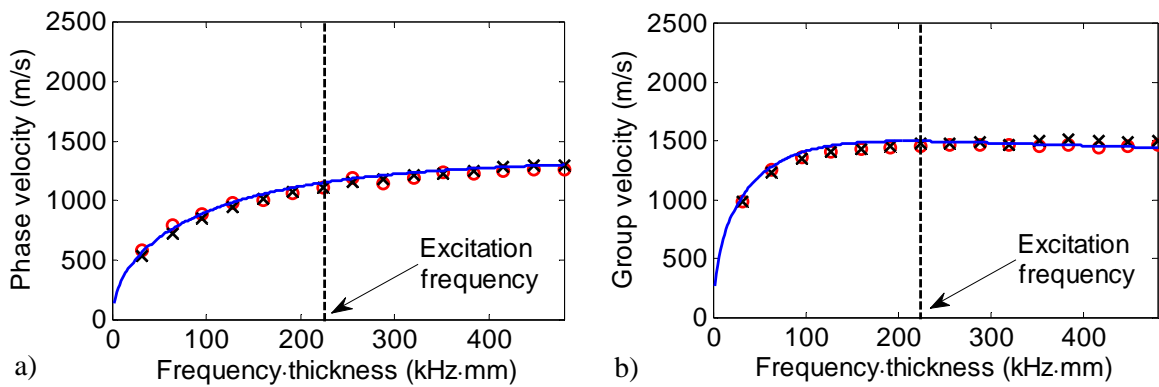
Fig 6. (a) Phase and (b) group velocity dispersion curves of the equivalent isotropic model calculated by analytical model (solid lines) and the QI composite laminate obtained from FE simulations (circles) and experimental measurements (crosses)
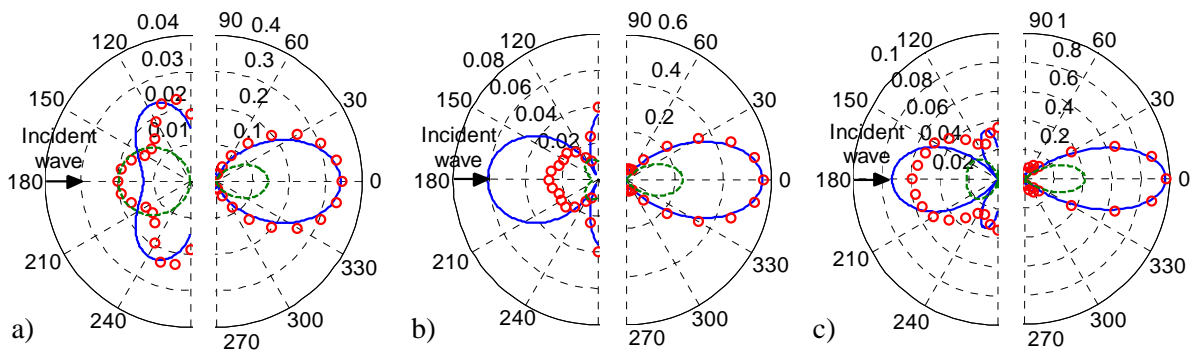

Fig 7. Analytical (solid lines), approximated (dashed lines) and FE (circles) results for SDP of delaminations with R = (a) 0.85, (b) 1.09 and (c) 1.46 and located at mid-thickness of the equivalent isotropic model

a) $R_{EI} = 0.85$, $R_{QI} = 0.88$ b) $R_{EI} = 1.03$, $R_{QI} = 1.07$ c) $R_{EI} = 1.46$, $R_{QI} = 1.51$
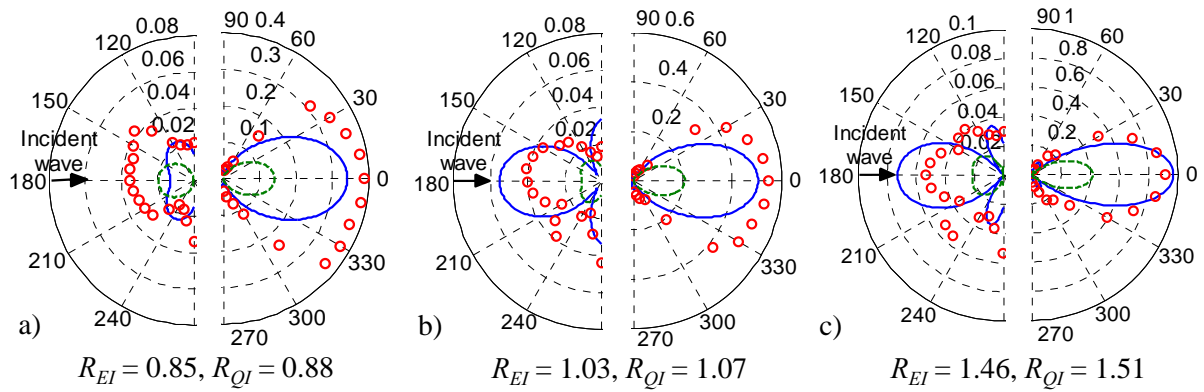
Fig 8. Analytical (solid lines), approximated (dashed lines) and FE equivalent isotropic model (circles) and QI composite laminate model (crosses) results of normalised forward scattered wave amplitudes at θ = (a) 0°, (b) 20° and (c) 40° as a function of R for delaminations located at mid-thickness of the equivalent isotropic model, crosses are FE results of the QI composite laminate
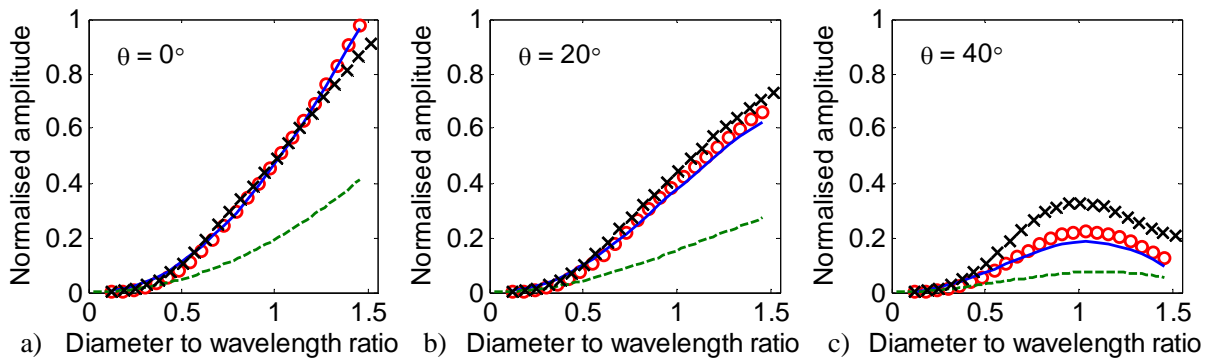

a) Diameter to wavelength ratio b) Diameter to wavelength ratio c) Diameter to wavelength ratio

Fig 9. Analytical (solid lines), approximated (dashed lines) and FE equivalent isotropic model (circles) and QI composite laminate model (crosses) results of normalised backward scattered wave amplitudes at θ = (a) 180°, (b) 200° and (c) 220° as a function of R for delaminations located at mid-thickness of the equivalent isotropic model, circles are FE results of the QI composite laminate
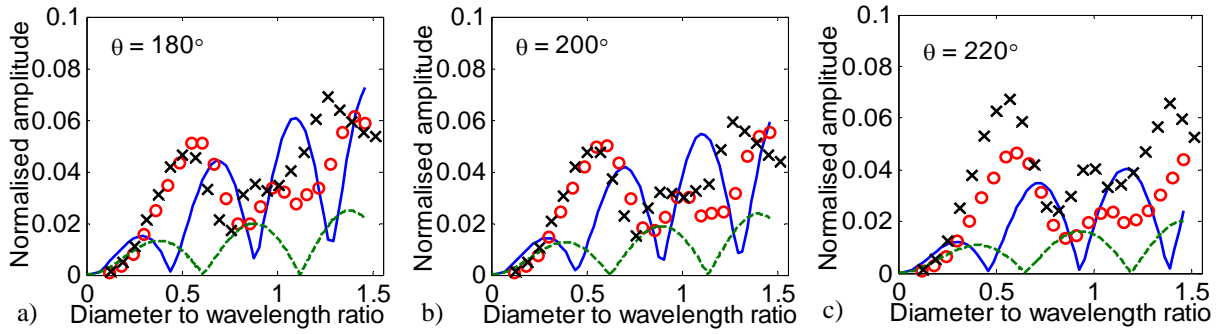
Fig 10. Analytical (solid lines) and approximated (dashed lines) results for SDP of delaminations located at mid-thickness of the equivalent isotropic model, circles are FE results of the QI composite laminate
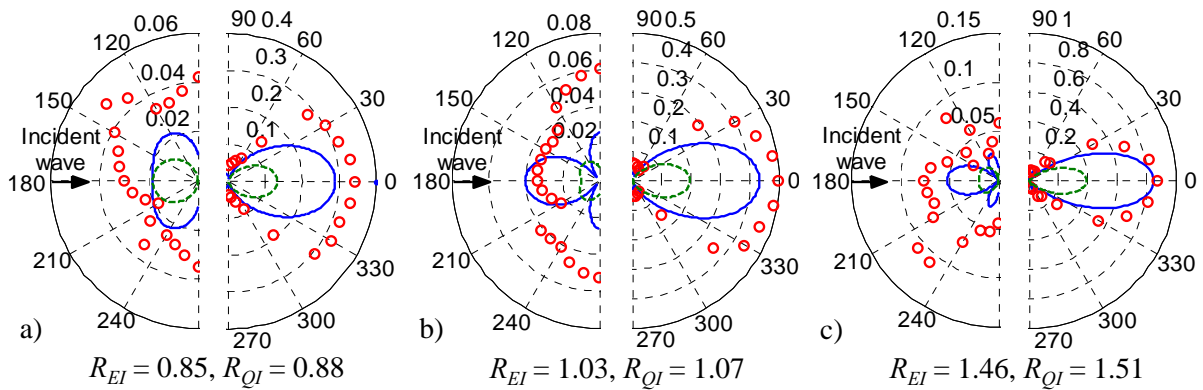

Fig 11. Analytical (solid lines) and approximated (dashed lines) results for SDP of delaminations located between 3rd and 4th lamina in the equivalent isotropic model, circles are FE results of the QI composite laminate